AIAA JOURNAL
Vol. 34, No. 7, July 1996

Performance of Three-Dimensional Compressible Navier–Stokes Codes at Low Mach Numbers

William E. Milholen II* and Ndaona Chokani†
North Carolina State University, Raleigh, North Carolina 27695-7910
and
J. Al-Saadi‡
NASA Langley Research Center, Hampton, Virginia 23681-0001

The low-Mach-number performance of two widely used three-dimensional compressible Navier–Stokes solvers is examined. Both of the codes employ a finite volume formulation, but differ in their respective discretization and solution schemes. In the first code, a central-difference discretization is employed and solutions are obtained using an explicit Runge–Kutta time-stepping scheme. In the second code, an upwind-biased discretization is used, and an implicit approximate factorization scheme is employed. The accuracy and efficiency of the codes are assessed by comparison with results from an incompressible Navier–Stokes solver and experimental data. The test cases examined include an untwisted rectangular wing and a wing–fuselage configuration. The computed pressure distributions were nearly identical, and agreed quite well with experimental data. In addition, the predicted pressure distributions were nearly identical to those predicted by the incompressible flow-solver. The influence of freestream Mach number on the efficiency of both compressible-flow solvers also is examined.

Nomenclature

C_D	= drag coefficient
C_L	= lift coefficient
C_p	= surface static pressure coefficient
c	= local chord length
M	= Mach number
N	= total number of grid points
N_c	= number of grid points with Mach number >0.30
Re	= Reynolds number based on mean geometric chord
u, v, w	= velocity components in the x, y, z directions
u^+	= incompressible law-of-the-wall velocity, u/u_τ
u_τ	= incompressible friction velocity, $\sqrt{(\tau_w/\rho_\infty)}$
v	= total velocity magnitude
x, y, z	= Cartesian coordinate system
x/c	= nondimensional chord fraction
y^+	= incompressible law-of-the-wall coordinate, yu_τ/ν_∞
α	= angle-of-attack, deg
ζ	= normal coordinate to wing surface
η	= nondimensional semispan fraction
ν	= kinematic velocity
ρ	= density
τ_w	= wall shear stress

Subscripts

f	= final value
∞	= freestream value

Introduction

COMPUTATIONAL fluid dynamics has previously been motivated by the need to accurately and efficiently obtain solutions for compressible-flow problems. The progress made over the past decade has made it possible to accurately predict compressible three-dimensional viscous flows over complex configurations. As a consequence, methods for solving the three-dimensional incompressible Navier–Stokes equations have only recently become efficient. For this reason, compressible flow solvers are still often used to simulate low-speed flows.

This present work was motivated by the current interest in the design and optimization of high-lift systems using Navier–Stokes solvers.[1] The flowfields of interest are typical of takeoff and landing conditions, with freestream Mach numbers of approximately 0.20. Even though the freestream Mach numbers of interest are low, the flow around a transport wing with high-lift devices deployed may contain regions of supersonic flow.[2] Thus, to properly model the flow physics, a compressible-flow solver may be required. However, the application of a compressible-flow solver at low Mach numbers can be problematic.

At low freestream Mach numbers, the performance of a compressible flow solver can be expected to degrade to the point where either the solver becomes inefficient, or accurate solutions may be unobtainable.[3,4] The inefficiency stems from the fact that the allowable local time step is inversely proportional to the local speed of sound.[5] As the freestream Mach number decreases, the speed of sound increases, and the allowable time step decreases. As a result, solution times increase. Also, in the limit as the freestream Mach number goes to zero, the solution of the compressible-flow equations becomes singular.[6] For these reasons, it is necessary to examine the low-Mach-number performance of a particular flow solver to determine where it becomes inefficient or inaccurate.

Recently, several researchers investigated the performance of compressible-flow solvers at low freestream Mach numbers.[3,4] Although quite informative, the geometries used for the computations were two-dimensional. The objective of this paper is to compare the low-Mach-number performance of two widely used three-dimensional compressible Navier–Stokes solvers. For comparison, results obtained from an incompressible Navier–Stokes solver also are presented. The compressible Navier–Stokes solvers chosen, TLNS3D-MB[7] (TLNS3D) and CFL3D,[8] represent the current state of the art of compressible three-dimensional Navier–Stokes solvers. The incompressible Navier–Stokes solver, INS3D-UP[9] (INS3D), represents the current state of the art of incompressible Navier–Stokes solvers.

The performance of the two compressible-flow solvers is evaluated using the following approach. Two geometries of practical

Presented as Paper 95-0767 at the AIAA 33rd Aerospace Sciences Meeting, Reno, NV, Jan. 9–12, 1995; received Sept. 15, 1995; revision received Feb. 12, 1996; accepted for publication Feb. 12, 1996.

*Graduate Research Assistant, Department of Mechanical and Aerospace Engineering; currently National Research Council Research Associate, NASA Langley Research Center, Hampton, VA 23681. Student Member AIAA.

†Associate Professor, Department of Mechanical and Aerospace Engineering. Member AIAA.

‡Research Engineer, Aerodynamics Division.

engineering interest are examined. The first geometry is an untwisted rectangular wing.[10] The second geometry is a subsonic transport wing–fuselage configuration.[11] The accuracy of the computational results is examined by making direct comparison to available experimental data. In particular, the influence of freestream Mach number on the efficiency of the compressible-flow solvers is examined in detail.

Computational Codes

The three computational codes used in the present research are discussed briefly below. Both compressible-flow solvers, TLNS3D and CFL3D, were developed at NASA Langley Research Center. The incompressible-flow solver, INS3D, was developed at NASA Ames Research Center. Both TLNS3D and CFL3D are finite volume codes, whereas INS3D is a finite difference code.

TLNS3D solves the three-dimensional, time-dependent, thin-layer compressible Navier–Stokes equations for a body-fitted coordinate system.[7] The equations are discretized in a central-difference, finite volume formulation. The solution is advanced to steady state using an explicit Runge–Kutta time-stepping scheme that is second-order accurate. Artificial dissipation in the form of blended second and fourth differences is added for stability. The artificial dissipation can be added in either scalar or matrix form. For the present research, only the matrix form of artificial dissipation is employed. Additional details of the code can be found in Ref. 7. CFL3D solves the time-dependent, thin-layer, compressible Navier–Stokes equations for a body-fitted coordinate system.[8] The equations are discretized using an upwind-biased, finite volume formulation. The convective and pressure terms are upwind biased using the flux–difference splitting scheme of Roe. The shear stress and heat transfer terms are centrally differenced. The solution is implicitly advanced to steady state by use of a three-factor approximate factorization that is second-order accurate. Thomas et al.[8] give additional details of CFL3D. For steady-state solutions, both TLNS3D and CFL3D take advantage of several acceleration techniques, including multigridding, grid sequencing, and local time-stepping. INS3D solves the incompressible Navier–Stokes equations for a body-fitted coordinate system, using the method of artificial compressibility.[9] The equations are discretized using an upwind-biased finite difference formulation. The convective, pressure, and shear stress terms are treated similarly to those of CFL3D. The solution is implicitly advanced to steady state using a Gauss–Seidel-type line relaxation scheme. The resulting solution is second-order accurate. Further details of the code can be found in Ref. 9.

All three Navier–Stokes solvers discussed above offer several turbulence modeling options. For the present research, only the one-equation model of Spalart–Allmaras[10] is used to simulate the effects of fine-scale turbulence. This turbulence model has become available only recently in INS3D, and results obtained with this present version should be interpreted cautiously. For all test cases presented, fully turbulent flow was simulated.

To consistently compare the convergence characteristics of the codes, the lift coefficient was monitored. When the lift coefficient converged to four decimal places, the solutions were considered converged. In addition, the computation time was monitored to compare computational efficiency.

Experimental Data

The results obtained from all three Navier–Stokes solvers were validated by making comparison to experimental data. Two geometries of practical interest are considered. The first geometry[11] is an untwisted rectangular wing with an aspect ratio of 6.0. The wing cross section is the NACA 0012 airfoil. The tests were conducted at a freestream dynamic pressure of 30.0 psf, which corresponds to a freestream Mach number of 0.14 and Reynolds number of 3.17×10^6. The wing was well instrumented with surface pressure taps at 10 spanwise stations. The manufacturer's stated accuracy for the electronically scanned pressure system was ± 0.72 psf. In addition, force and moment data are available. The second geometry is a subsonic transport wing–fuselage configuration.[12] The wing has an aspect ratio of 10.0, with a quarter-chord sweep angle of 27.0 deg and a 5.0-deg dihedral angle. The wing is constructed of supercritical airfoil sections, with a nonlinear twist distribution. The tests were conducted at a freestream Mach number of 0.20, at a stagnation pressure of 5.0 atm. The corresponding Reynolds number was 4.20×10^6, with a dynamic pressure of 260.0 psf. The experimental data consist of force and moment data, along with wing-pressure data at three spanwise stations. The wing surface pressures were measured by ± 15.0-psi differential pressure transducers and four 48-port scanning valves.

Results and Discussion

Figure 1 shows a partial view of the C-O grid used for the rectangular wing geometry. An algebraic grid-generation algorithm based on transfinite interpolation was used to generate the three-dimensional grid. Grid points have been clustered where large flow gradients exist in the chordwise, spanwise, and normal directions. For this wing geometry, the upstream and downstream boundaries extend eight root-chord lengths from the leading and trailing edges of the wing, respectively. Figure 2 shows a partial view of the single block C-O grid topology used for the wing–fuselage configuration. The grid was generated using GRIDGEN.[13] The upstream and downstream boundaries extend six semispan lengths, which corresponds to approximately 18 wing root-chord lengths. Because no side slip was considered, symmetry conditions were applied at the root plane of each grid.

Rectangular Wing Computations

A grid refinement study was conducted for the simple wing configuration using all three codes. Figure 3 compares computed

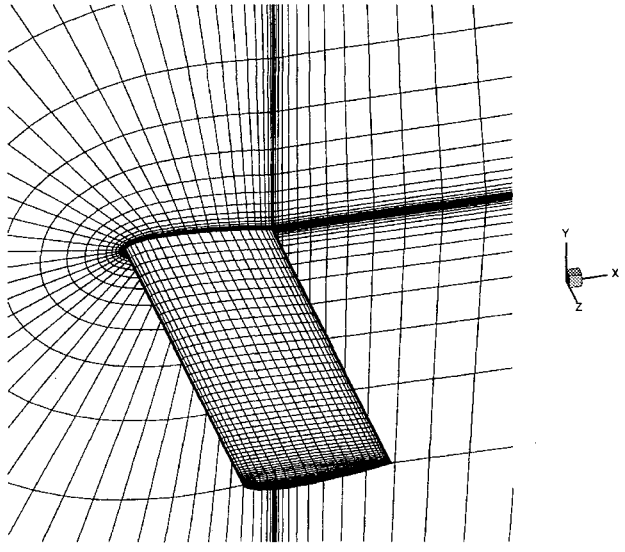

Fig. 1 Partial view of rectangular wing C-O grid.

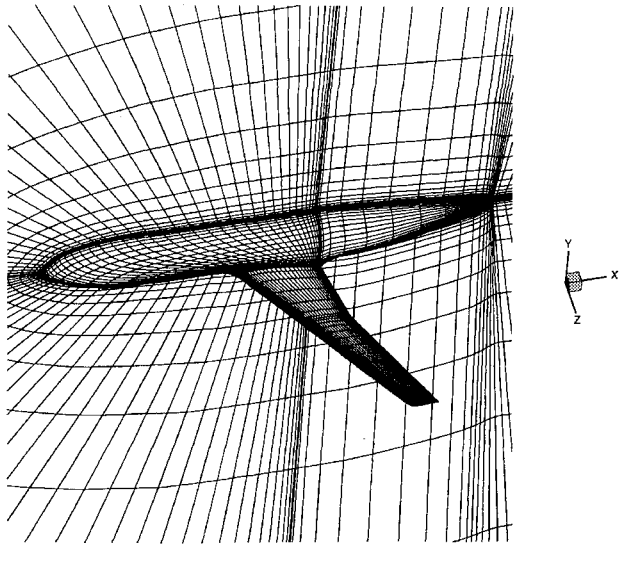

Fig. 2 Partial view of transport wing-fuselage C-O grid.

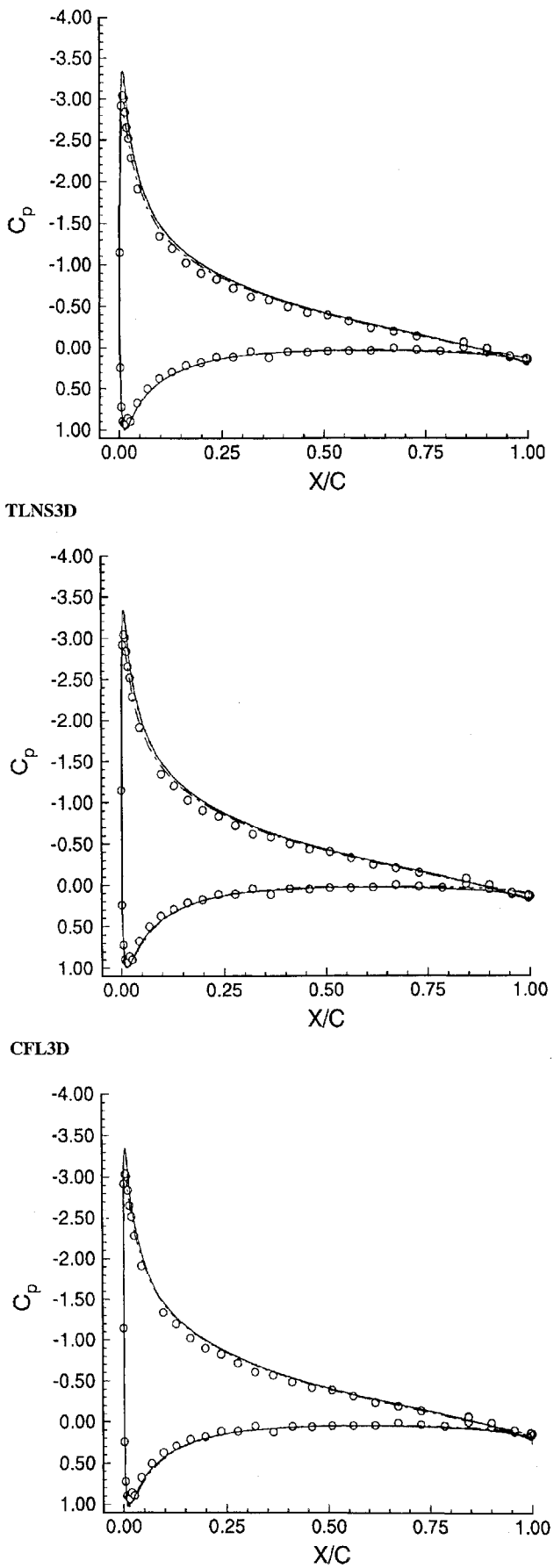

Fig. 3 Influence of grid refinement on rectangular wing pressure distribution: η = 0.6084 (M_∞ = 0.14, α = 10.01 deg, Re = 3.17 × 10^6): ○, experiment; ——, 289 × 73 × 73; - - - -, 193 × 49 × 49; and – – –, 97 × 25 × 25.

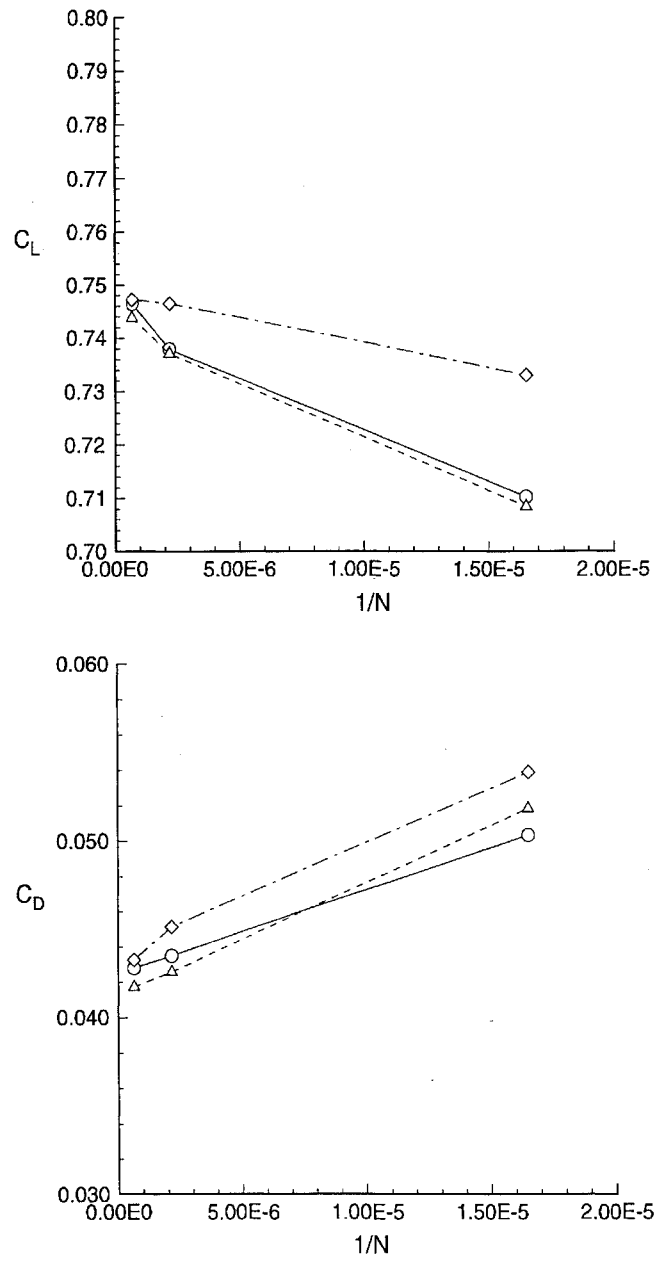

Fig. 4 Influence of grid refinement on rectangular wing lift and drag coefficients (M_∞ = 0.14, α = 10.01 deg, Re = 3.17 × 10^6): ○, TLNS3D; △, CFL3D; and ◇, INS3D.

pressure distributions obtained from three representative grids to experimental data at one spanwise location. These computations simulated fully turbulent flow, using the Spalart–Allmaras turbulence model. The grid dimensions, such as 193 × 49 × 49, represent the number of grid points in the streamwise, normal, and spanwise directions, respectively. Refinement of the grid improves the agreement with experimental data, particularly in the leading-edge region. The results obtained using the 289 × 73 × 73 grid are identical within plotting accuracy to those obtained using the 193 × 49 × 49 grid for all three codes. Figure 4 shows the influence of grid refinement on computed lift and drag coefficients. On the two finest grids, the maximum variation in lift coefficient for both compressible-flow solvers is 1.1%, whereas for INS3D, the variation is only 0.1%. The maximum variation in drag coefficient for both compressible-flow solvers is 2.0%, whereas for INS3D, the variation is approximately 4.3%. Figure 5 shows the influence of grid refinement on upper-surface streamwise velocity profiles at the 50% chord location at the same spanwise location. Again, the results from the two finer grids are nearly identical. From this grid refinement study, it is evident that the 193 × 49 × 49 grid is capable of adequately resolving the features of the flowfield. This grid was used for the subsequent

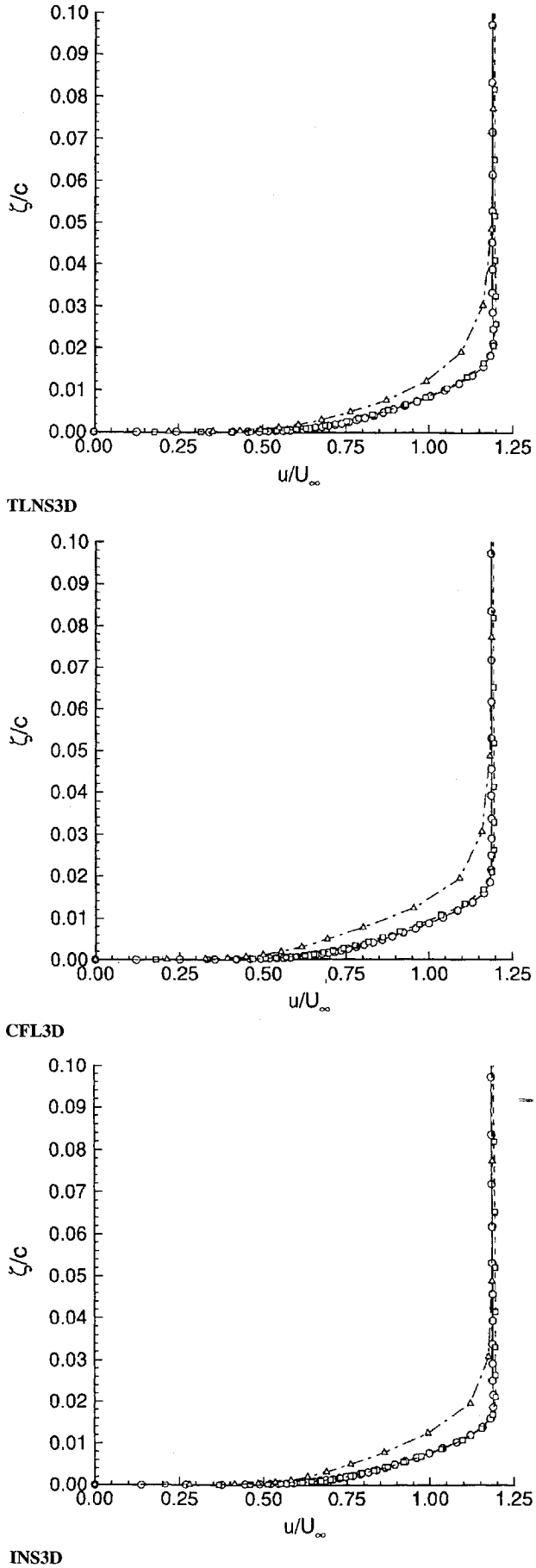

Fig. 5 Influence of grid refinement on rectangular wing upper-surface streamwise velocity profile at $x/c = 0.50$, $\eta = 0.6084$ ($M_\infty = 0.14$, $\alpha = 10.01$ deg, $Re = 3.17 \times 10^6$): ○, 289 × 73 × 73; □, 193 × 49 × 49; and △, 97 × 25 × 25.

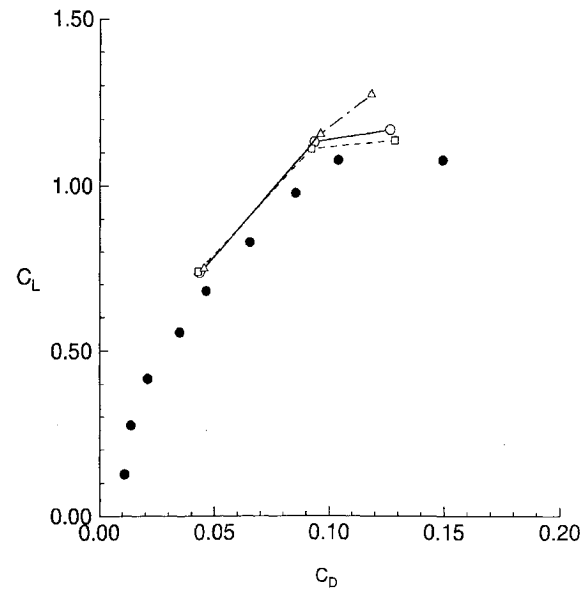

Fig. 6 Comparison of predicted and experimental rectangular wing drag polars ($M_\infty = 0.14$, $Re = 3.17 \times 10^6$): •, experiment; ○, TLNS3D; □, CFL3D; and △, INS3D.

computations. With this grid, typical values of y^+ for the first grid point off of the wing surface were in the range of 1–5, with approximately 25 grid points clustered in the wing boundary layer.

Figure 6 compares computed and experimental drag polars. The computations were performed at the following angles of attack: 10.01, 16.00, and 18.10 deg. In general, the agreement with the experimental data is good. The three codes agree well at the two lower angles of attack. However, INS3D underpredicts the flow separation at the highest angle of attack. Subsequent computations with INS3D have shown that the choice of turbulence model has a strong impact on the predicted flow separation. Given this result, detailed comparison of the computational results from all three flow solvers are presented only at the lower angle of attack, where all three codes have predicted attached flow.

Figure 7 compares predicted pressure distributions to experimental data at three spanwise stations for $\alpha = 10.01$ deg. Across the span of the wing, all three flow solvers accurately predict the leading-edge suction peaks, and their associated adverse pressure gradients. At the two inboard stations, the computational results are nearly identical, and agree quite well with the experimental data. At the outboard station, the influence of the tip vortex on the upper surface is consistently underpredicted. The computations, however, are still in good qualitative agreement with the data. Note that the computed spanwise load distributions were nearly identical.[14]

Figure 8a compares computed upper-surface streamwise velocity profiles in physical coordinates at 50% chord, and $\eta = 0.6084$. The similarities among the profiles are encouraging. Outside of the boundary layer, all codes predict nearly identical flow acceleration over the wing. Inside the boundary layer, small differences are observed. The profile predicted by INS3D is slightly fuller, and thus more resistant to flow separation. This result may partially account for the underprediction of flow separation by INS3D at the higher angles of attack, as discussed above. The velocity profiles in incompressible wall coordinates are shown in Fig. 8b. This comparison confirms that the differences in the boundary-layer profiles in the inner region are small. In the outer region, the differences between the compressible and incompressible results arise because of the higher wall shear stress predicted by INS3D. Similar observations were made at other locations.

Figure 9 compares the convergence histories of lift and drag coefficients from all three flow solvers. The normalized coefficients are plotted relative to Cray Y-MP CPU time in hours. The arrows indicate where the lift coefficient has converged to 99.5% of its final value. Using this criterion, the drag coefficient is also similarly converged. The computational time of CFL3D is approximately

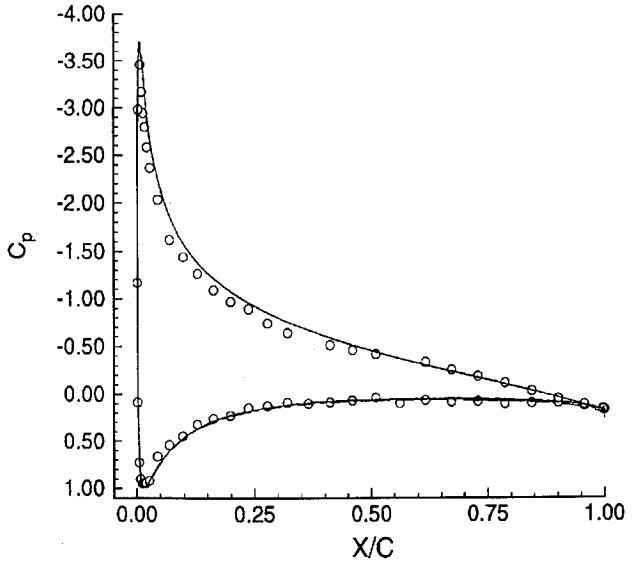

$\eta = 0.3436$

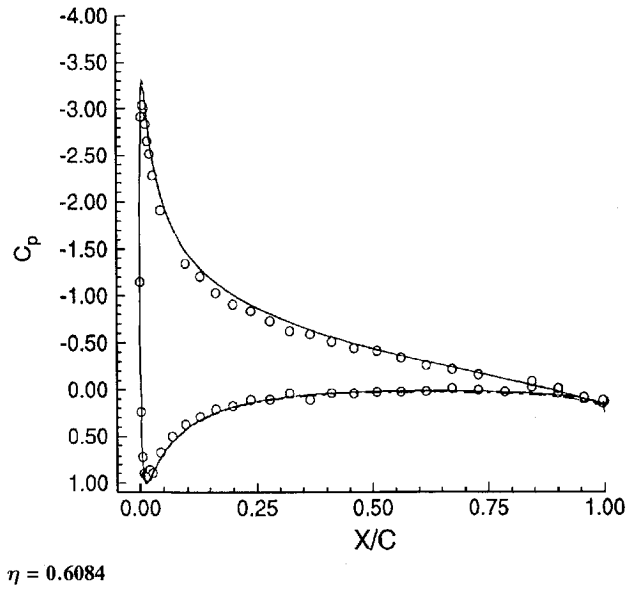

$\eta = 0.6084$

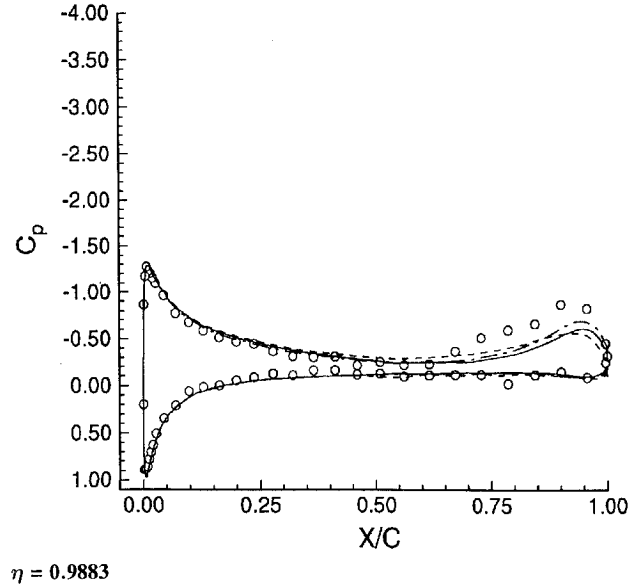

$\eta = 0.9883$

Fig. 7 Comparison of predicted and experimental rectangular wing pressure distributions ($M_\infty = 0.14$, $\alpha = 10.01$ deg, $Re = 3.17 \times 10^6$): ○, experiment; ——, TLNS3D; - - - -, CFL3D; and – – –, INS3D.

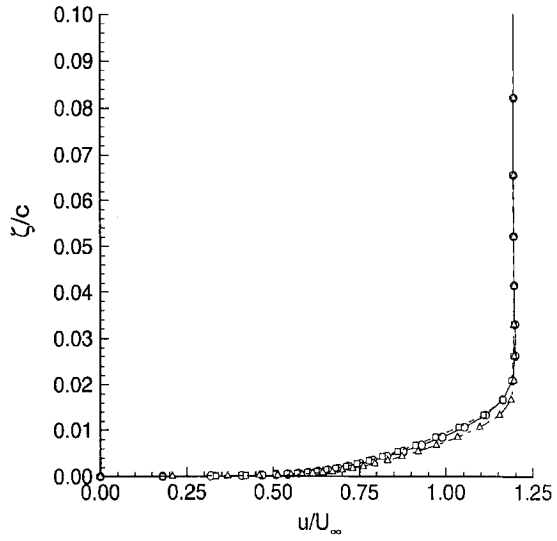

a) Physical coordinates

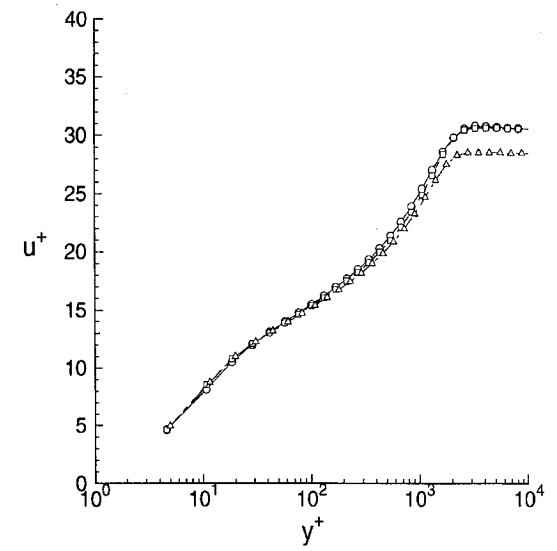

b) Wall coordinates

Fig. 8 Comparison of rectangular wing upper-surface streamwise velocity profiles $x/c = 0.50$, $\eta = 0.6084$ ($M_\infty = 0.14$, $\alpha = 10.01$ deg, $Re = 3.17 \times 10^6$): ○, TLNS3D; □, CFL3D; and △, INS3D.

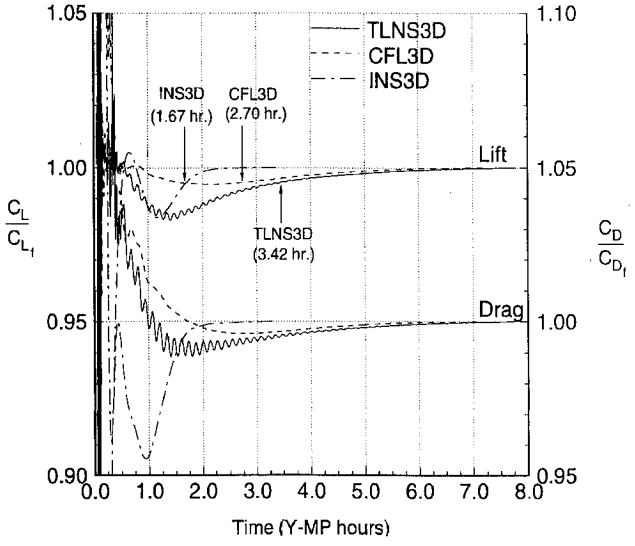

Fig. 9 Comparison of rectangular wing convergence histories ($M_\infty = 0.14$, $\alpha = 10.01$ deg, $Re = 3.17 \times 10^6$).

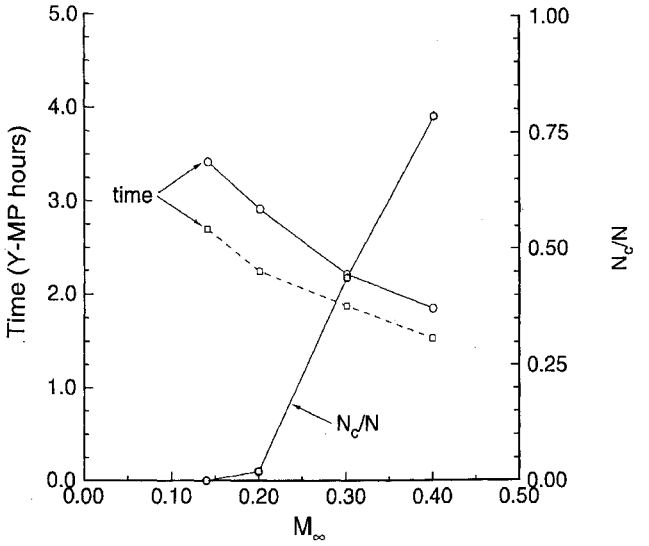

Fig. 10 Influence of freestream Mach number on rectangular wing solution time (α = 10.01 deg, Re = 3.17 × 10^6): ○, TLNS3D and □, CFL3D.

60% higher than that of INS3D, whereas the computational time of TLNS3D is approximately twice that of INS3D.

The influence of freestream Mach number on the efficiency of both compressible-flow solvers is examined using the following approach. The angle of attack and Reynolds number are held constant, but the freestream Mach number is varied. For this study, the following freestream Mach numbers were chosen: 0.14, 0.20, 0.30, and 0.40. In Fig. 10, the computational times required for the lift coefficient to converge to 99.5% of its final value are plotted vs the freestream Mach number. Also shown as a measure of flowfield compressibility is the fraction of grid points with a Mach number greater than 0.30. As the freestream Mach number decreases, the predicted flowfields change significantly, ranging from compressible to largely incompressible. As the freestream Mach number decreases, the computational times increase significantly, on the order of 75%. Consistently, CFL3D is more efficient, requiring approximately 20% less CPU time than TLNS3D at the lowest freestream Mach number examined. The INS3D solution for this angle of attack required 1.67 h, which is approximately 60% less than that of CFL3D at $M_\infty = 0.14$.

Transport Wing–Fuselage Computations

A grid refinement study was conducted for the transport wing–fuselage configuration using only TLNS3D. For the sake of brevity, these results are not presented. From this grid-refinement study, it was clear that a 241 × 65 × 81 grid was capable of resolving the features of the flowfield. The resulting wing grid is 145 × 61. With this grid, typical values of y^+ for the first grid point off of the wing surface and fuselage surface were in the range of 1–5, with approximately 25 grid points clustered in the boundary layer.

Figure 11 compares computed pressure distributions to experimental data at three spanwise locations. These computations simulated fully turbulent flow, using the Spalart–Allmaras turbulence model. The computations agree quite well with the experimental data. Across the span of the wing, all three flow solvers again accurately predict the leading-edge suction peaks and the subsequent adverse pressure gradients. The predicted lower surface pressure distributions are identical to within plotting accuracy. On the upper wing surface, small differences are observed. At all stations, INS3D predicts slightly stronger adverse pressure gradients aft of the leading-edge suction peak. Again, the computed spanwise load distributions were found to be nearly identical.[14]

Figure 12a compares predicted upper-surface streamwise velocity profiles in physical coordinates at 50% chord, and $\eta = 0.6234$. Again, the profiles are quite similar. INS3D predicts that the external flow is slightly decelerated, compared to the results from both compressible-flow solvers. This result is consistent with the stronger

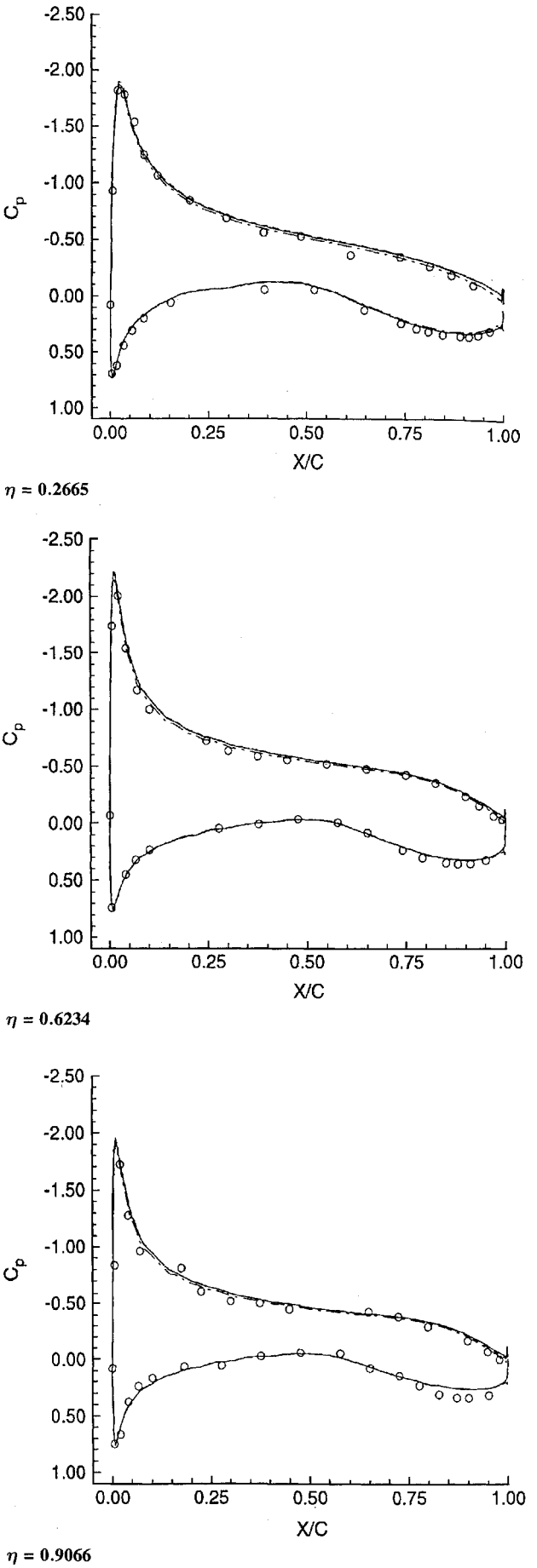

Fig. 11 Comparison of predicted and experimental transport wing pressure distributions (M_∞ = 0.20, α = 4.43 deg, Re = 4.20 × 10^6): ○, experiment; ——, TLNS3D; - - - -, CFL3D; and – – –, INS3D.

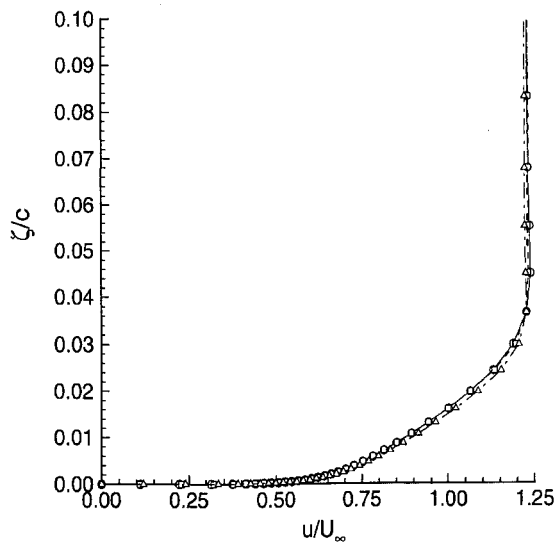

a) Physical coordinates

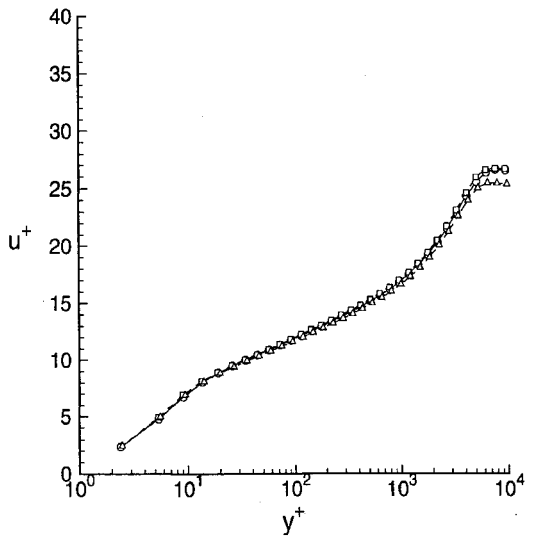

b) Wall coordinates

Fig. 12 Comparison of transport wing upper-surface streamwise velocity profiles at $x/c = 0.50$, $\eta = 0.6234$ ($M_\infty = 0.20$, $\alpha = 4.43$ deg, $Re = 4.20 \times 10^6$): ○, TLNS3D; □, CFL3D; and △ INS3D.

adverse pressure gradients predicted by INS3D, as discussed above. Inside the boundary layer, INS3D again predicts a slightly fuller profile. The profiles in incompressible wall coordinates are shown in Fig 12b. Again, the profiles are nearly identical in the inner region. Similar observations were made at other locations.

The computational times required for the lift coefficient to converge to 99.5% of its final value were quite different. On a Cray C-90 supercomputer, TLNS3D required 1.9 h, CFL3D required 2.1 h and INS3D required 2.7 h. This is in sharp contrast to the rectangular wing computational times discussed above, where both compressible-flow solvers required significantly more computational time than INS3D. For this test case, INS3D required approximately 40% more computational time than TLNS3D. These results show that the relative computational times are case dependent.

Conclusions

The low-Mach-number performance of two widely used three-dimensional compressible Navier–Stokes solvers is examined. Two geometries of practical engineering interest are examined. The first geometry is an untwisted rectangular wing, and the second is a subsonic transport wing–fuselage configuration. The results of this research provide guidance in evaluating the low-Mach-number performance of compressible-flow solvers.

Both compressible-flow solvers accurately predicted the low-speed flow over both geometries. The computed pressure distributions were nearly identical, and agreed well with the experimental data. Also, the predicted pressure distributions were nearly identical to those predicted by the incompressible-flow solver. In addition, predicted boundary-layer profiles from all three flow solvers were quite similar.

The computational efficiency of the three flow solvers was examined by monitoring the computational times. For the rectangular wing, both compressible-flow solvers required significantly more computational time for the lift coefficient to converge to 99.5% of its final value, compared to the incompressible-flow solver. For the subsonic transport wing–fuselage configuration, this trend was reversed, with the incompressible-flow solver requiring more computational time. This shows that the computational times are case dependent.

The influence of freestream Mach number on the efficiency of both compressible-flow solvers was examined. As the freestream Mach number decreased from 0.40 to 0.14, the computed flowfields changed significantly, ranging from compressible to largely incompressible. Over this Mach-number range, the computational times increased on the order of 75%.

Acknowledgments

This work was supported by Cooperative Agreement NCC1-169 between North Carolina State University and the Research Facilities Branch at NASA Langley Research Center. The authors are grateful to L. Elwood Putnam for his support of this work. The authors acknowledge Veer N. Vatsa, Christopher L. Rumsey, and Stuart E. Rogers for many helpful and insightful discussions regarding the use of the three Navier–Stokes solvers. The authors thank Zachary T. Applin for providing experimental data for the rectangular wing. The computations were performed on the North Carolina Supercomputing Center's Cray Y-MP and the Numerical Aerodynamic Simulation Facility's Cray C-90.

References

[1]Meredith, P. T., "Viscous Phenomena Affecting High-Lift Systems and Suggestions for Future CFD Development," AGARD CP-515, Oct. 1992, pp. 19.1–19-8.

[2]Squire, L. C., "Interactions Between Wakes and Boundary-Layers," *Progress in Aerospace Science*, Vol. 26, No. 3, 1989, pp. 261–288.

[3]Volpe, G., "Performance of Compressible Flow Codes at Low Mach Numbers," *AIAA Journal*, Vol. 31, No. 1, 1993, pp. 49–56 (AIAA Paper 91-1662, June 1991).

[4]Choi, Y. H., and Merkle, C. L., "The Application of Preconditioning in Viscous Flows," *Journal of Computational Physics*, Vol. 105, No. 2, 1993, pp. 207–223.

[5]Anderson, D. A., Tannehill, J. C., and Pletcher, R. H., *Computational Fluid Mechanics and Heat Transfer*, Hemisphere, New York, 1984, Chap. 9, pp. 479–518.

[6]Pletcher, R. H., and Chen, K. H., "On Solving the Compressible Navier–Stokes Equations for Unsteady Flows at Very Low Mach Numbers," AIAA Paper 93-3368, July 1993.

[7]Vatsa, V. N., Sanetrik, M. D., and Parlette, E. B., "Development of a Flexible and Efficient Multigrid-Based Multiblock Flow Solver," AIAA Paper 93-0677, Jan. 1993.

[8]Thomas, J. L., Taylor, S. L., and Anderson, W. K., "Navier–Stokes Computations of Vortical Flows over Low Aspect Ratio Wings," AIAA Paper 87-0207, Jan. 1987.

[9]Rogers, S. E., Kwak, D., and Kiris, C., "Numerical Solution of the Incompressible Navier–Stokes Equations for Steady-State and Time-Dependent Problems," *AIAA Journal*, Vol. 29, No. 4, 1991, pp. 603–610 (AIAA Paper 89-0463, Jan. 1989).

[10]Spalart, P. R., and Allmaras, S. R., "A One-Equation Turbulence Model for Aerodynamic Flows," AIAA Paper 92-0439, Jan. 1992.

[11]Applin, Z. T., "Pressure Distributions from Subsonic Tests of a NACA 0012 Semispan Wing Model," NASA TM 110148, Sept. 1995.

[12]Morgan, H. L., Jr., "Model Geometry Description and Pressure Distribution Data from Tests of EET High-Lift Research Model Equipped with Full-Span and Part-Span Flaps," NASA TM 80048, Feb. 1979.

[13]Steinbrenner, J. P., and Chawner, J. R., "Incorporation of a Hierarchical Grid Component Structure into GRIDGEN," AIAA Paper 93-0429, Jan. 1993.

[14]Milholen, W. E., II, and Chokani, N., "Low Mach Number Performance of Three-Dimensional Compressible Navier–Stokes Codes," AIAA Paper 95-0767, Jan. 1995.